ARTICLES
https://doi.org/10.1038/s41565-020-00805-z
nature nanotechnology



# Micelle-enabled self-assembly of porous and monolithic carbon membranes for bioelectronic interfaces

Yin Fang[1,9]✉, Aleksander Prominski[1,2,9], Menahem Y. Rotenberg[2,9], Lingyuan Meng[3,9], Héctor Acarón Ledesma[4,9], Yingying Lv[2], Jiping Yue[1], Erik Schaumann[1,2], Junyoung Jeong[5], Naomi Yamamoto[1], Yuanwen Jiang[1,2], Benayahu Elbaz[6], Wei Wei[7] and Bozhi Tian[1,2,8]✉

**Real-world bioelectronics applications, including drug delivery systems, biosensing and electrical modulation of tissues and organs, largely require biointerfaces at the macroscopic level. However, traditional macroscale bioelectronic electrodes usually exhibit invasive or power-inefficient architectures, inability to form uniform and subcellular interfaces, or faradaic reactions at electrode surfaces. Here, we develop a micelle-enabled self-assembly approach for a binder-free and carbon-based monolithic device, aimed at large-scale bioelectronic interfaces. The device incorporates a multi-scale porous material architecture, an interdigitated microelectrode layout and a supercapacitor-like performance. In cell training processes, we use the device to modulate the contraction rate of primary cardiomyocytes at the subcellular level to target frequency in vitro. We also achieve capacitive control of the electrophysiology in isolated hearts, retinal tissues and sciatic nerves, as well as bioelectronic cardiac sensing. Our results support the exploration of device platforms already used in energy research to identify new opportunities in bioelectronics.**

Modern bioelectronics with multi-scale structures are used extensively for drug delivery, biosensing and biological modulations[1–4]. Through modulation of biological activities, these bioelectronics have contributed to our improved understanding of biological dynamics and function. Moreover, they hold great therapeutic potential for treating many biological disorders, including Parkinson's disease, congenital heart defects and paralysis. However, macroscopic bioelectronic devices are usually rigid and mechanically invasive to cells and tissues. Their large feature sizes also make subcellular biointerfaces difficult to form. Many devices also display faradaic reactions at the electrode surfaces, which can generate toxic reactive species, corrode electrodes and cause permanent damage to adjacent tissues[5].

Nanostructuring of the bioelectronics surfaces represents a promising way to improve the device performance[6]. Standard bioelectronic stimulation materials, such as platinum, iridium oxide or titanium nitride, all display enhanced charge injection limits when their surfaces become nanostructured or porous[7]. Nanostructured conducting polymer-based bioelectronics, such as those based on poly(3,4-ethylenedioxythiophene) polystyrene sulfonate (PEDOT:PSS), are also widely used for biological interfaces, and they show internal porosity, great electronic/ionic conductivity, high volumetric capacitance and excellent mechanical properties[8,9]. Improvements are ongoing to make these polymer electrodes electrochemically more stable, especially in terms of repeated operation and swelling during long-term soaking in saline solution[10,11]. Besides, electrode surface coating with carbon nanomaterials, such as graphene and carbon nanotubes, is widely used to reduce the impedance at the electrode–saline junctions and increase the charge transfer rate[12–14]. However, the polymer binding process usually associated with carbon coating procedures may result in 'dead' volumes or surfaces and increased total device thickness[15]. Moreover, the potential production of free-standing carbon nanostructures after dissociation of the coating layer may result in biological complications in vivo[16,17]. Carbon nanostructures have nevertheless been advancing modern electronics[12–17] in multiple areas, such as supercapacitor[18,19] or micro-supercapacitor-based[20] power elements, as well as stretchable or bendable microelectrodes for biointerfaces[3,7,21–23]. Therefore, there are still numerous opportunities to further advance carbon-based materials towards cheap, stable, minimally invasive, high-performance and multifunctional bioelectronic devices.

In this Article, we aim to integrate many key features of advanced biointerface-forming electrodes into carbon-based bioelectronic devices, such as the surface and internal porosity, mechanical compliance and use of nanomaterial building blocks for bottom-up construction. We rely on micelle-enabled self-assembly to prepare a binder-free (that is, monolithic), carbon-based and flexible micro-supercapacitor-like system for various types of bioelectronic interfaces. The monolithic carbon minimizes the biocompatibility complication associated with free-standing carbon nanostructures. The interdigitated electrode design shrinks the feature size of the otherwise bulky electrode for subcellular interfaces. The devices can operate under either micro-supercapacitor-like or a traditional

[1]Department of Chemistry, University of Chicago, Chicago, IL, USA. [2]The James Franck Institute, University of Chicago, Chicago, IL, USA. [3]Pritzker School of Molecular Engineering, University of Chicago, Chicago, IL, USA. [4]The Graduate Program in Biophysical Sciences, University of Chicago, Chicago, IL, USA. [5]Department of Computer Science, University of Chicago, Chicago, IL, USA. [6]The Division of Multiple Sclerosis and Neuroimmunology, Feinberg School of Medicine, Northwestern University, Chicago, IL, USA. [7]Department of Neurobiology, University of Chicago, Chicago, IL, USA. [8]Institute for Biophysical Dynamics, University of Chicago, Chicago, IL, USA. [9]These authors contributed equally: Yin Fang, Aleksander Prominski, Menahem Y. Rotenberg, Lingyuan Meng, Héctor Acarón Ledesma. ✉e-mail: yinfang@nano-theranostic.com; btian@uchicago.edu

monopolar electrode configuration under physiological conditions, yielding modulation of cardiomyocytes (CMs) in vitro, excitation of isolated heart and retinal tissues ex vivo and stimulation of sciatic nerves in vivo, as well as bioelectronic cardiac recording.

## Carbon membrane synthesis and characterization

We adopted a bottom-up approach for the direct preparation of monolithic (that is, binder-free) and hierarchical carbon membranes. Nanoscale micelles were prepared through biphasic interaction between triblock copolymer Pluronic F127 (the primary organic template) and resin (the primary carbon precursor) in ethanol. The micelle solution was spin-coated onto the thermal oxide silicon wafer. Following solvent-evaporation-induced self-assembly (Fig. 1a(i)), the packed micelles were carbonized completely into mesoporous carbon membranes. The carbonization process leads to the cross-linking of carbon precursors and the formation of monolithic membrane structures. The process yields highly ordered mesostructures, as shown in transmission electron microscopy images (Fig. 1b and Supplementary Fig. 1). Nitrogen adsorption/desorption measurements further showed a narrow pore size distribution of ~7 nm (Supplementary Fig. 2).

To reduce the stiffness of carbon films for improved compliance with soft biological interfaces, we introduced an inorganic template for the creation of a macroporous layer. Addition of ~200–300-nm-sized silica ($SiO_2$) spheres coated with dopamine into the Pluronic F127 and resin mixture during the membrane preparation (Fig. 1a(ii)) introduced macroporous (that is, with pore size >50 nm) structures (Fig. 1c and Supplementary Figs. 3 and 4). The role of dopamine here is to stabilize the dispersion of $SiO_2$ spheres in the micelle solution and to provide an additional carbon source. The hierarchical porous carbon preparation scheme permitted layer-by-layer assembly (Fig. 1a(iii)) of mesoporous carbon by spin-coating, where the thickness and porosity of individual layers can be controlled. Subsequent buffered hydrofluoric acid treatment removes the $SiO_2$ templates and releases the membrane (Supplementary Fig. 5). While the mesoporous film had a Young's modulus and hardness of 25.30 GPa and 3.82 GPa, respectively, an addition of ~700 nm of the macroporous layer reduced these values to 4.20 GPa and 0.69 GPa (Fig. 1d). We hypothesized that electrochemical devices made from highly porous layers may deliver efficient capacitive currents that may be useful for biological modulation when biointerfaces are formed (Fig. 1e)[24].

## Device fabrication and characterization

We fabricated the device in a micro-supercapacitor-like design and over an SU-8 substrate. The SU-8 thin film is chosen because it is photo-patternable, mechanically flexible and chemically stable, and it has been commonly applied as a substrate or encapsulation material in flexible electronics[25,26]. Since SU-8 is incompatible with the carbonization conditions under high temperature, all photolithography processes have to be performed on the fully carbonized membrane. To avoid difficult substrate transfer steps, we followed an 'upside-down' fabrication method (Fig. 2a and Supplementary Fig. 6), where the last step releases the device from the substrate and exposes the side for potential biointerfaces (that is, the original interface between the thermal oxide and the carbon; Fig. 1a(iii)). This fabrication technique requires that the softer layer (that is, the layer that forms direct biointerfaces) be on the bottom of the as-made membrane; hence the layer-by-layer assembly has to start from the layer that yields macropores. We used patterned metals as the mask for carbon etching as well as the electrical conductor to the carbon-based porous biointerfaces. By shrinking the pad size for interdigitated patterns, we were able to produce multi-channel micro-supercapacitor-like devices (Supplementary Fig. 5). Raman spectra mapping showed carbon peaks at 1,330 and 1,590 $cm^{-1}$ only in the patterned region, confirming the presence of a carbon membrane (Fig. 2c).

Mechanical simulations for puncture deformation showed that compared to the uniformly covered multilayered device, the interdigitated pattern can reduce the maximum von Mises stress present in both the carbon and metal layers, suggesting a mechanical justification of the micro-supercapacitor-like device (Supplementary Fig. 7). We also performed electrostatics simulations to model the electric potential at the surface of the device and between the interdigitated electrodes (Supplementary Fig. 8). Comparing a two-prong and a ten-prong electrode model with the same total electrode area, the ten-prong electrode geometry yields a more confined electrical potential distribution at the cross-section. This is reminiscent of the local return electrode designs for photovoltaic devices used for retinal implants[27]. We speculate that this confined *z*-axis electrical potential may be beneficial for stimulation of cell monolayers in vitro or tissues with multilayered circuit organization (for example, retina).

Next, we conducted electrochemical tests using several physiological electrolytes. The electrochemical performance of the porous carbon membranes was analysed by cyclic voltammetry (CV) and galvanostatic charge/discharge techniques (Fig. 2d,e and Supplementary Figs. 9–12). In $Na_2SO_4$ electrolyte solution, the device showed near-rectangular CV profiles up to a scan rate of 100 mV $s^{-1}$ (Supplementary Fig. 9), confirming that the device acted as an electrostatic double-layer capacitor. Notably, the devices also showed a near-rectangular CV profile in Dulbecco's Modified Eagle Medium (DMEM) up to a scan rate of 100 mV $s^{-1}$, demonstrating that the capacitor behaviour was maintained even in cell culture media (Fig. 2d). Areal specific capacitances calculated from the CV profiles (Supplementary Fig. 9) were comparable to those of other supercapacitors or micro-supercapacitors[28–30] (Supplementary Table 1). Electrochemical impedance spectroscopy tests revealed low equivalent resistances of ~680 Ω and 715 Ω of the device in phosphate-buffered saline (PBS) and DMEM solutions, respectively (Supplementary Fig. 13), suggesting good charge transport properties. Without optimization, the charge injection limit of the device is estimated to be at least ~120 μC $cm^{-2}$ (Supplementary Fig. 14), which is comparable to Pt and Pt/Ir alloy electrodes used in tissue stimulations (Supplementary Table 2). Additionally, the electrode preserved a near-rectangular CV profile with a scan rate up to 4 V $s^{-1}$ (Supplementary Fig. 15).

Lastly, the intrinsic device stability in physiological solution was tested by submerging the device in 37 °C PBS solution for one month, during which no obvious change in capacitance was observed (Fig. 2f). The device showed electrochemical and mechanical stabilities over the course of at least 1,000,000 uninterrupted cycles (Fig. 2g and Supplementary Figs. 15 and 16). Together, these results demonstrate that the device is promising for bioelectronic interfaces.

## Biological training in vitro

We first confirmed the viability of CMs and primary rat cardiac fibroblasts cultured on the device surface. Live–dead assays showed that ~100% of CMs were still alive after a three-day culture (Supplementary Fig. 17). Rat cardiac fibroblast nuclear staining on the device showed healthy nucleus morphology, and no obvious nuclear changes due to cell death or apoptosis were observed (Supplementary Fig. 18). To have a more sensitive evaluation of the device in vitro biocompatibility, we conducted the lactate dehydrogenase (LDH) cytotoxicity assay using rat cardiac fibroblasts. The LDH cytotoxicity percentages in the SU-8 group on day 1 (mean value, 3.91%) and day 2 (mean value, 2.97%) indicate that SU-8 alone caused a very mild cytotoxicity in vitro, although SU-8 is widely recognized as a biocompatible material[25,26]. When all the device materials are present (that is, SU-8, porous carbon and metals), the LDH percentages are 8.77% (mean) and 4.93% (mean)

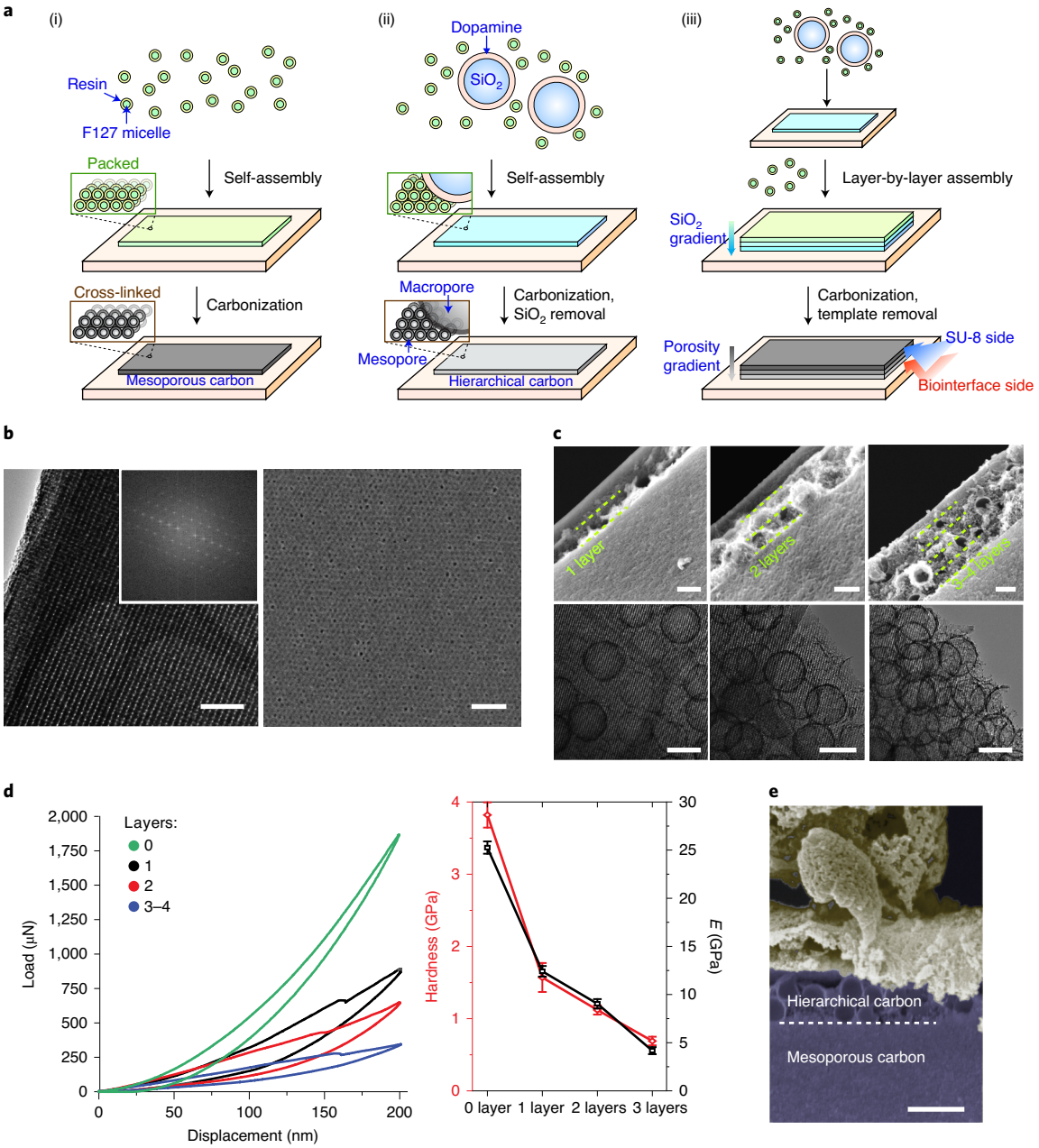


**Fig. 1 | Hierarchical porous carbon synthesis and characterization. a**, Illustration of the preparation of hierarchical porous carbon. (i) Synthesis of mesoporous carbon; (ii) synthesis of hierarchical carbon containing both mesopores and macropores; (iii) layer-by-layer assembly of carbon layers creating a porosity gradient. The bottom layer of the carbon membranes will become the side for biointerface formation after the device fabrication is completed (Fig. 2a and Supplementary Fig. 6). **b**, Transmission electron microscopy (left; scale bar, 100 nm), corresponding fast Fourier transform (left inset) and scanning electron microscopy (SEM) images (right; scale bar, 100 nm) of mesoporous materials showing the highly ordered mesostructures. **c**, Cross-sectional view (upper panels) and associated top view (lower panels) of the hierarchical porous material. The hierarchical structures display two components: a bottom layer constructed from an ordered mesoporous structure and layers of porous vesicles assembled into multiple layers (as separated by the dashed lines). Scale bar, 200 nm. **d**, Left: representative load versus displacement plots of the hierarchical porous thin film measured with a nano-indenter. Each sample has 0, 1, 2 or 3–4 macropore layers. The experiment was repeated four times at various locations on each sample. Right: hardness and Young's modulus calculated from the load versus displacement plots (mean ± s.e.m., $n = 4$ independent measurements at various locations on each kind of sample). As the number of layers increases, the Young's modulus and hardness decrease, indicating that the film becomes softer. **e**, Cross-sectional (false colour) SEM image of CMs cultured on the hierarchical porous film. Scale bar, 500 nm. Results in **b**, **c** and **e** are representative of five independent repeats.

for day 1 and day 2, respectively. However, the LDH levels in both the SU-8 and the device groups decreased on day 2 versus on day 1, suggesting that the cellular tolerance for these synthetic materials increased over time.

Haematoxylin and eosin stain of mice skin tissues surrounding the implanted devices showed that subcutaneous implantation caused some mild histological changes in weeks 1 and 4 (Supplementary Fig. 19). No substantial inflammation reactions

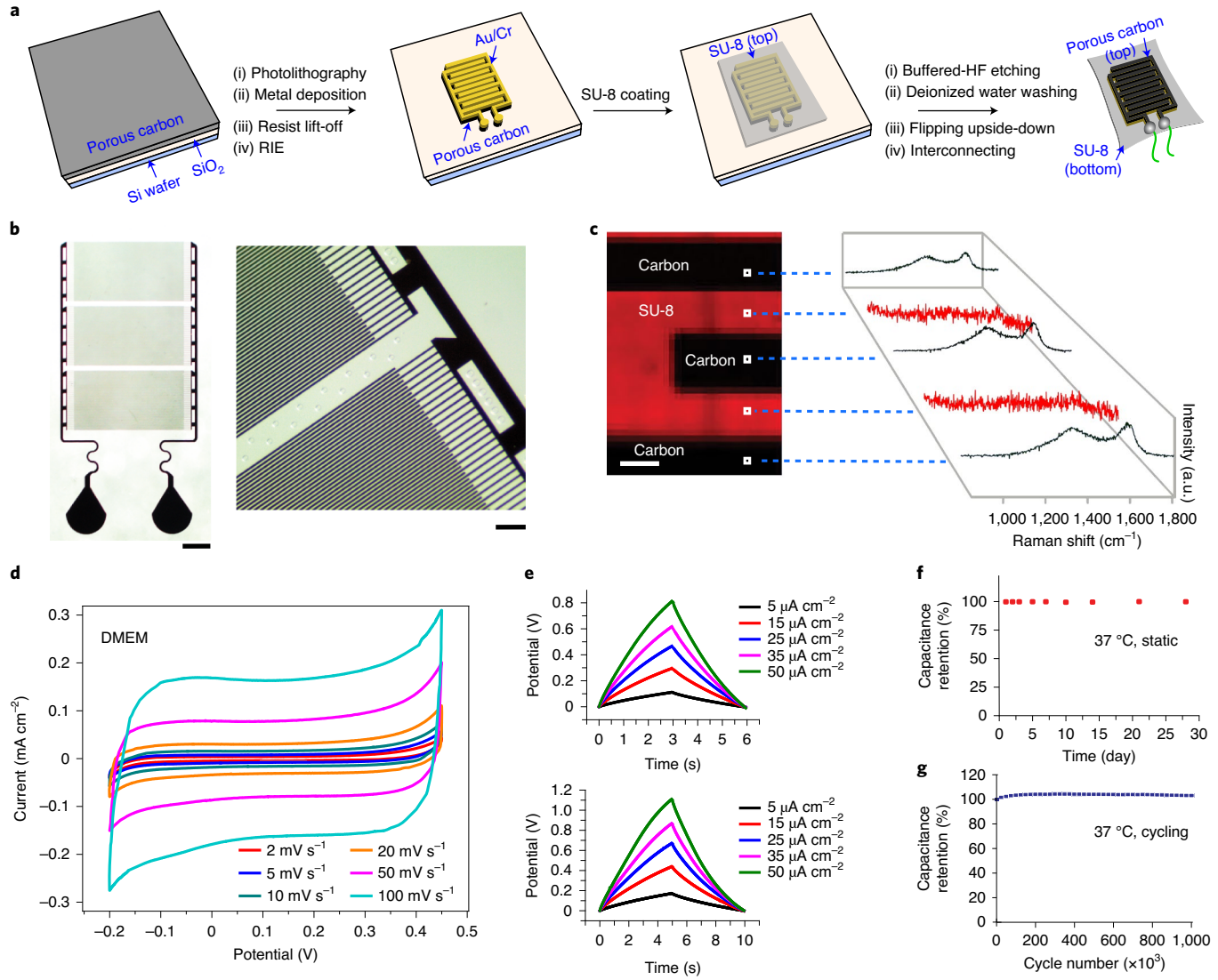


**Fig. 2 | Device fabrication and characterization. a**, Overview of a flexible device fabrication workflow. RIE, reactive-ion etching; HF, hydrofluoric acid. **b**, An optical image (left; scale bar, 1 mm) and a close-up view of the hierarchical porous carbon micro-supercapacitor device (right; scale bar, 200 μm). Photographs are representative of more than twenty devices that were fabricated. **c**, Raman spectra for the micro-supercapacitor device at the indicated locations (left; scale bar, 10 μm). The spectra showing typical carbon peaks at around 1,330 $cm^{-1}$ and 1,590 $cm^{-1}$ are found only in the designed pattern region (right). **d**, CV profiles for the micro-supercapacitor at different scan rates in cell culture medium DMEM. **e**, Charge/discharge curves in DMEM of the micro-supercapacitor device at different current densities for the time window of 6 s (top) and 10 s (bottom). **f**, Electrochemical stability of the device during storage at 37 °C in a buffer solution (PBS) over a one-month period. **g**, Electrochemical stability over 1,000,000 CV cycles in the range −0.1 to 0.1 V at the frequency of 4 Hz at 37 °C in a buffer solution (PBS).

or tissue damage was observed. The histological appearance of the skin tissue above the implanted device (that is, the epidermis and the dermis) was normal in week 4, except for the mild thickening of subcutaneous connective tissue and mild recruitment of immune cells including macrophages and neutrophils. Additionally, we monitored mouse body weight, and no weight loss was observed between control groups and device groups (Supplementary Fig. 19).

We analysed the formation of a biointerface between the device and the cultured CMs by verification of the expression of typical cardiac markers, such as cardiac troponin and connexin-43 (Fig. 3a). We additionally confirmed that cells could spread out on the device surface and form subcellular interfaces (Supplementary Figs. 20 and 21). To evaluate how the charging/discharging cycles from the micro-supercapacitor-like device affect the CM electrophysiology, we applied the stimulation current to the CM-interfacing devices and performed simultaneous calcium imaging to monitor cellular electrical activity. Each side of the interdigitated electrodes acts as a lead, and a square current waveform is applied between them (Methods for details). Prior to stimulation, CMs were synchronized with a baseline beating rate of ~0.67 Hz. Upon application of an input electric current waveform, overdrive pacing was achieved, and the contraction rate immediately synchronized to the pacing frequency (Fig. 3b and large field of view in Supplementary Fig. 23). It is noteworthy that the pacing rate doubles that of the stimulation rate (that is, the applied current frequency; 0.5 Hz pacing rate in Supplementary Fig. 22; 1 Hz pacing rate in Fig. 3b and Supplementary Fig. 23). This is expected as both the anodic and the cathodic phases of the electrochemical stimulation (from the same finger electrode area) can excite the CMs, although

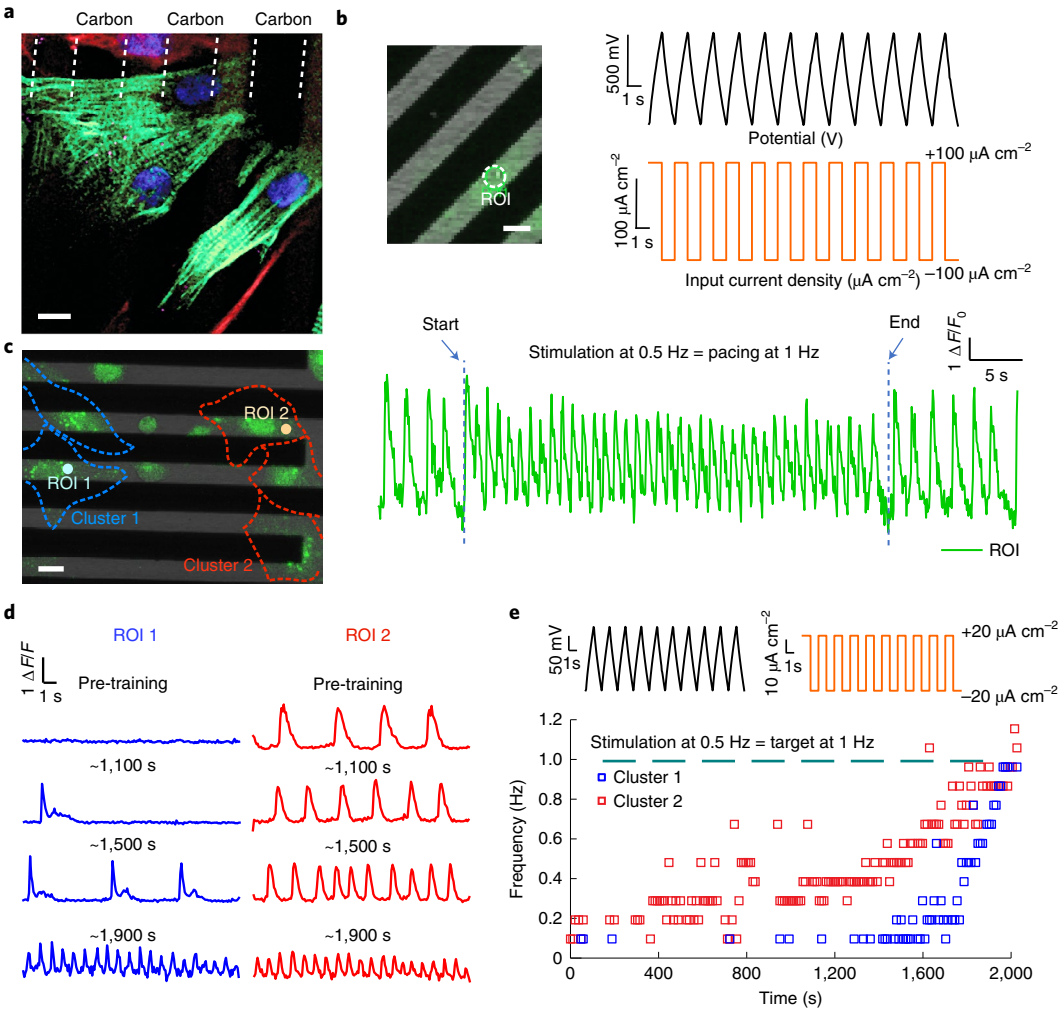


**Fig. 3 | In vitro biological training. a**, Representative immunohistochemistry images for cardiac cells cultured on the micro-supercapacitor device. Cells were stained for cardiac troponin (CMs, green), connexin-43 (magenta), vimentin (fibroblasts, red) and 4′,6-diamidino-2-phenylindole (DAPI; nuclei, blue). Dashed lines, the edges of the interdigitated carbon electrodes. Scale bar, 10 μm. The experiment was repeated twice with similar results. **b**, Upper left: representative image of CMs loaded with calcium sensitive dye; transmitted light shows the micro-supercapacitor (appears in black). Scale bar, 10 μm. Upper right: device voltage (top) and input current density (bottom) during the stimulation. Bottom: cell contraction rate illustrated by plotting the intensity profile of the ROI (highlighted in the image). Overdrive stimulation was reproduced with similar results in three independent experiments. **c**, Representative image of CMs loaded with calcium sensitive dye recorded during subthreshold stimulation for 2,000 s. Scale bar, 10 μm. Overlay shows approximate positions of CMs in the field of view, and their cluster assignment was colour-coded in blue (cluster 1) and red (cluster 2). **d**, Representative traces of fluorescence intensities at the ROI (dots in panel **c**) at the beginning of experiment and at 1,100, 1,500 and 1,900 s of stimulation. Microphotographs (**c**) and cell trainings (**d**) in subthreshold pacing are representative of three independent experiments. **e**, Frequency analysis of cell contraction frequency during subthreshold training. Top panel shows the voltage (left) and the input current density (right) waveforms during the training process. Bottom: frequency analysis shows fluctuating but gradual increase in the contraction rate, which eventually reached the target training frequency of 1 Hz.

the action potentials (APs) may be initiated at different subcellular locations. One advantage of the electrical stimulation from the interdigitated layout is that it can achieve direct cell modulation uniformly across the entire device area. Also, the confined electrical potential around the finger electrodes may help improve the efficiency of stimulation as CM cultures are typically monolayer, and it may be unnecessary to deliver an electric field far above the cell surface.

Although this ability to perform overdrive pacing of CMs may have promising therapeutic applications, we also wanted to demonstrate the utility of the device for in vitro cellular manipulation that would allow for basic mechanistic investigations. To this end, we applied current stimulation with subthreshold amplitude, which did not elicit a direct overdrive pacing response. Figure 3c shows a field of view in which five CMs synchronized in two clusters were identified with very low spontaneous activity (~0.2 Hz and 0 Hz). When a low amplitude current waveform was applied (one fifth of the overdrive pacing current), the CMs did not show an immediate response. However, when the stimulation was applied for a longer duration, a gradual increase in contraction frequency was observed. After ~1,900 s of stimulation, the cells were evidently 'upregulated' by the current stimulation, and their contraction rate increased to the target stimulation rate of 1 Hz. Figure 3d shows representative calcium imaging traces from two regions of interest (ROIs), before and during the training of the two cell clusters, and Fig. 3e shows a gradual increase in contraction frequency over time. These results resemble the gradual increase in the rate of electrical activity previously observed in CMs upon subthreshold optical stimulation[31].

While the cells within each cluster are synchronized throughout the training, the two clusters display negligible synchronization to each other before they reach the targeted frequency (Supplementary Fig. 24 and Supplementary Videos 1 and 2). This fact suggests that the subthreshold training displays cellular level heterogeneity and the stochastic events may be involved in this process. Although a detailed understanding of the precise underlying mechanism here requires further rigorous investigation, we postulate that repetitive stimulation alters the resting membrane potential of the CMs to the point that they are sufficiently depolarized to elicit APs. A possible mechanism might relate to the 'memory effect', which refers to the way supra-threshold stimulation alters the excitability of cells and their resulting resting frequency[32]. Because the porous carbon-based devices operate via capacitive charge injection, we were able to pace or train the CMs in a biocompatible way without generating faradaic reactions. Purely capacitive operation reduces undesirable processes such as electrode corrosion, which can cause device failure.

## Biological modulation at the tissue and organ levels

Intact neural tissues represent highly crowded environments that include non-neuronal factors, such as the extracellular matrix and glial interactions, that can influence neuronal activation. To determine whether the micro-supercapacitor-like device can modulate activity in intact neural circuits, we performed stimulation experiments on isolated mouse retinas. The laminated organization of the retina and its diverse neural circuit motifs make the retina an accessible model system to study brain circuit functions. Additionally, the use of retinal tissue allows us to stimulate physiologically relevant 'input neurons', that is, the photoreceptors, and record activity from the 'output neurons', that is, the retinal ganglion cells (RGCs) of a well-defined sensory circuit. In these experiments, we isolated retinas from transgenic mice that selectively express genetically encodable calcium indicator GCaMP6f in RGCs (*Slc17a6*$^{tm2(cre)Lowl}$/*Gt*(*ROSA*)*26Sor*$^{tm95.1(CAG-GCaMP6f)Hze}$)[33,34]. This enabled simultaneous monitoring of neural activity across multiple RGCs. Micro-supercapacitor-like devices and interconnects were fixed on glass coverslips using silicone glue and used as bottoms for the retina perfusion chamber. Dissected retinas were then positioned with the photoreceptor layer facing the micro-supercapacitor-like device and the RGC layer facing upward (Fig. 4a). Using two-photon laser scanning microscopy, we recorded calcium transients from RGCs while stimulating the photoreceptor layer with micro-supercapacitor modulation. We used square current waveforms applied to the interdigitated electrodes within the device to modulate the neural activity of the ganglion cell layer. Current flow direction was periodically switched by alternating between the anodic and cathodic phases every 3.5 s. Throughout the stimulation process, large periodic transients could be observed across several RGCs. During the anodic phase, RGCs exhibited large calcium transients, while during the cathodic phase, the calcium levels in RGCs returned to resting levels (Fig. 4b). To corroborate that the micro-supercapacitor stimulation observed was due to activation of the glutamatergic pathway from photoreceptors to bipolar cells to RGCs, we applied a cocktail of glutamate receptor antagonists, including 50 µM AP-5, 10 µM L-AP4 and 50 µM DNQX, to silence glutamate transmission in the retina. Upon the glutamate receptor blockade, the large calcium transients could no longer be observed in RGCs during micro-supercapacitor stimulation (Fig. 4c). These results demonstrated that the charging and discharging stimulation at the supercapacitor–photoreceptor interface evoked changes in glutamate release from photoreceptor neurons and could therefore activate the retinal network.

Next, we evaluated the bioelectronic stimulation in tissues and organs that required the traditional charge injection configuration. The rat heart contained a ~75-µm-thick epicardium separating the CMs and the device[35]. Therefore, a single micro-supercapacitor-like device was not sufficient to accumulate the depolarizing charge. In these experiments, one porous carbon-based device (that is, working electrode) was placed on the left ventricular (LV) wall of a rat heart to apply different current waveforms, while the other device was placed on the right ventricular (RV) wall (Fig. 4d). We found that the two porous carbon device configuration is highly efficient as both flexible devices form good contacts with the heart surface (Fig. 4e). We first applied anodic/cathodic current square waves with different frequencies as this can yield similar charging/discharging processes from a supercapacitor device (1 Hz, ±0.5 mA cm$^{-2}$, Fig. 4f; 1.67 Hz, ±0.4 mA cm$^{-2}$, Supplementary Fig. 25; 2 Hz, ±0.37 mA cm$^{-2}$, Fig. 4h; and 5 Hz, ±0.4 mA cm$^{-2}$, Supplementary Fig. 26). Upon stimulation, the heart immediately contracted at double the stimulation rate (Fig. 4f,h and Supplementary Video 3). This is similar to the observed in vitro pacing with a micro-supercapacitor device configuration, suggesting that both the anodic and cathodic stimulations from the working electrode can achieve a pacing effect. Due to the capacitive nature of our device and lack of faradaic charge injection, we hypothesize that the mechanism governing the electrical stimulation is similar to field coupling[36,37]. We observed positive/negative electrocardiogram (ECG) artefacts during the stimulation (Fig. 4f,g), while no artefact was associated with the spontaneous contraction. As the ECG was recorded from the aorta and the LV wall, the observed artefact may be attributed to the working electrode positioned on the LV wall. The artefact shapes and the positions are dependent on the device/ECG configurations, so they vary in different settings. As the elicited heart potentials were initiated near the onset of the anodic/cathodic phases of the square waves (Fig. 4h, left), we next shrank the duration for each phase while keeping the spacing of adjacent phases the same (that is, 250 ms; Supplementary Fig. 27). The results from the alternating anodic/cathodic pulses (5 ms; Fig. 4h, middle) show effective overdrive pacing with 3.7 µC cm$^{-2}$ charge injection per phase/pulse. Finally, we attempted the electrical pacing with conventional charge-balanced biphasic pulses and achieved efficient overdrive pacing at 0.7 µC cm$^{-2}$ charge injection in 1 ms pulse width (Fig. 4h, right).

Finally, to demonstrate the utility of the porous carbon-based device for in vivo neuro-modulation applications, we interfaced it with sciatic nerves. We used an acute setting in which the device was interfaced with the exposed nerve. When one device was interfaced with the sciatic nerve and the other device was interfaced with the rat's body, we observed that the associated limb was clearly moving with every cathodic phase of the current injection (Supplementary Video 4). This was further validated by electromyography recordings from the rat limb, which showed large potential spikes that were synchronized to the cathodic phase (Supplementary Fig. 28).

## Conclusion

In summary, we have developed a hierarchical carbon-based micro-supercapacitor-like device that is capable of biological modulation. The porous structures and the interdigitated designs improve the device mechanics and allow control over the current flow through capacitive charging/discharging. The device was successfully applied to in vitro, acute ex vivo and acute in vivo modulations with the capacitive charging/discharging cycles or traditional current pulses. The device also shows promise with respect to long-term stability and reasonable biocompatibility. Future device improvements include increasing the charge injection limit of the materials to match that of the best charge injection electrodes such as titanium nitride or iridium oxide[7]. Other functions of this micelle-based and self-assembled bioelectronics device may incorporate flexible electrical sensing, as shown preliminarily in the ECG recording from isolated hearts (Supplementary Fig. 29). Finally, while supercapacitors or micro-supercapacitors have been demonstrated in the past as implantable power elements, our findings suggest the utility of these designs for future bioelectric therapeutics.

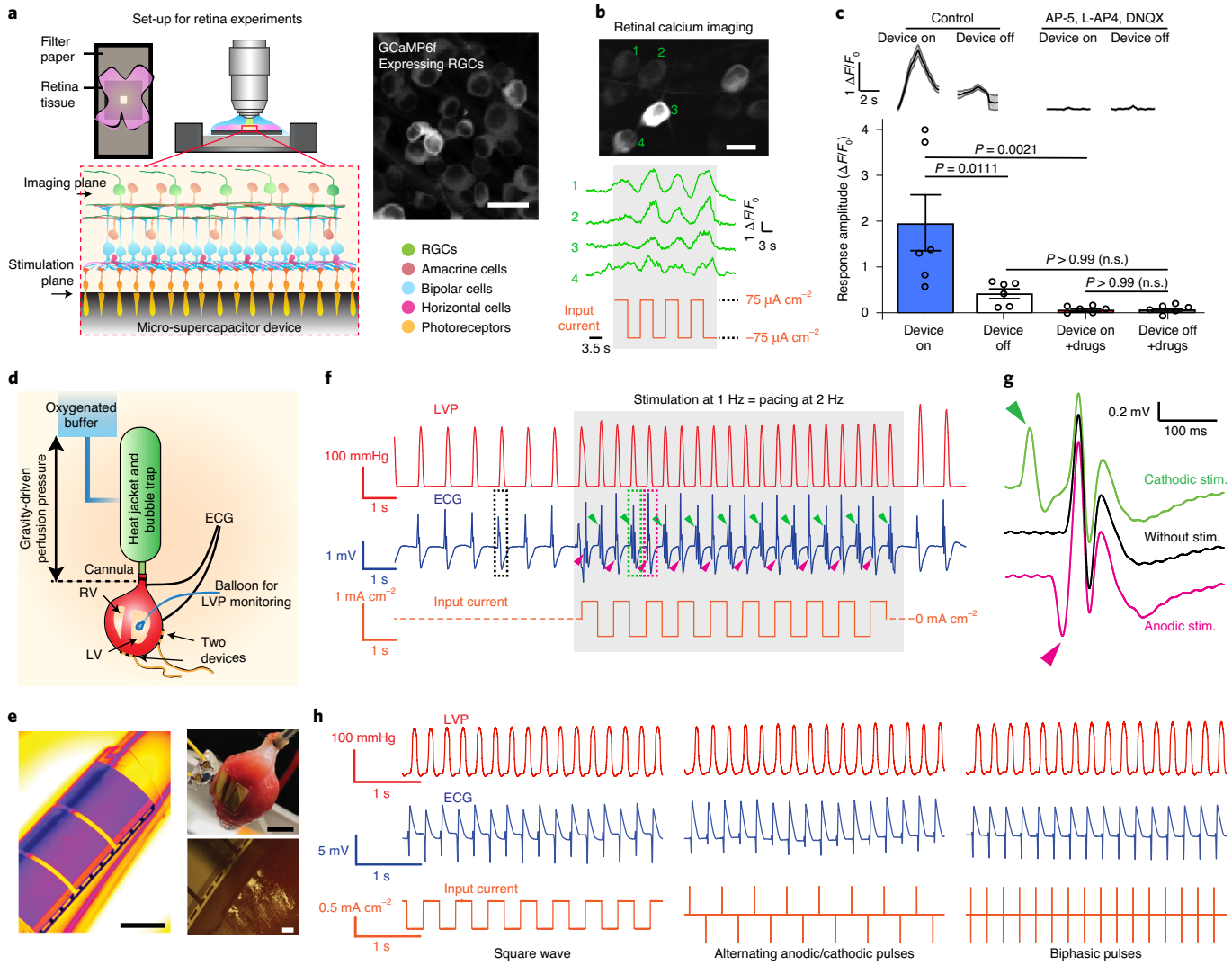


**Fig. 4 | Biological modulation at the tissue and organ level. a**, Left: schematic of the experimental set-up for the retinal stimulation. Right: a maximum-intensity projection of RGCs expressing GCaMP6f. Scale bar, 25 μm. **b**, Top: a retinal calcium image showing activated RGCs upon the stimulation. Scale bar, 15 μm. Middle: representative calcium traces from individual RGCs (numbered in the upper image). Bottom: the input current density during the stimulation. Confocal images in **a** and **b** are representative field of views from four repeats. **c**, Top: calcium transient traces represented as average ± standard error (s.e.m.) in both control and glutamate antagonist conditions. Bottom: the quantification of response amplitudes of calcium transients (mean ± s.e.m., $n = 6$ RGCs across various experimental conditions). Calcium transients from each RGC were averaged across five repeated measurements, and statistical analyses were performed using pairwise one-way analysis of variance with Bonferroni correction. Adjusted $P$ values are indicated in the plot; n.s., not significant. **d**, Schematic of the Langendorff perfusion system. ECG and left ventricular pressure (LVP) were monitored to show the effect of stimulation on the heart rate. **e**, Images of a micro-supercapacitor-like device conforming around a cylindrical holder (left; scale bar, 2 mm) and around the curvilinear and contractile cardiac tissue (upper right; scale bar, 5 mm) with a close-up view (lower right; scale bar, 500 μm). Images in **e** are representative of more than ten independent experiments. **f**, Representative LVP profiles and ECG recordings of the isolated heart stimulated at a frequency of 1 Hz. Input current density was synchronized to the corresponding stimulated portions of the LVP and ECG recordings. Dashed boxes and arrows are spontaneous APs (black) and APs that follow positive (green) and negative (pink) artefacts. **g**, A closer look at the APs in the ECG recording with corresponding colours; stim., stimulation. **h**, Representative LVP and ECG profiles of the isolated heart stimulated by 2 Hz square current waveform (left), 5 ms alternating pulses (middle) and 1 ms biphasic pulses (right) to achieve pacing at 4 Hz. Presented results from the isolated heart stimulation are representative of three independent experiments using independent hearts and electrodes.

## Online content

Any methods, additional references, Nature Research reporting summaries, source data, extended data, supplementary information, acknowledgements, peer review information; details of author contributions and competing interests; and statements of data and code availability are available at https://doi.org/10.1038/s41565-020-00805-z.

Received: 19 January 2020; Accepted: 26 October 2020;
Published online: 7 December 2020

## References

1. Someya, T., Bao, Z. & Malliaras, G. G. The rise of plastic bioelectronics. *Nature* **540**, 379–385 (2016).
2. Xie, Z., Avila, R., Huang, Y. & Rogers, J. A. Flexible and stretchable antennas for biointegrated electronics. *Adv. Mater.* **32**, 1902767 (2020).

3. Wang, L. et al. Functionalized helical fibre bundles of carbon nanotubes as electrochemical sensors for long-term in vivo monitoring of multiple disease biomarkers. *Nat. Biomed. Eng.* **4**, 159–171 (2020).
4. Huang, Z. et al. Three-dimensional integrated stretchable electronics. *Nat. Electron.* **1**, 473–480 (2018).
5. Zhirnov, V. V. & Cavin, R. K. *Microsystems for Bioelectronics: Scaling and Performance Limits* (William Andrew, 2015).
6. Acarón Ledesma, H. et al. An atlas of nano-enabled neural interfaces. *Nat. Nanotechnol.* **14**, 645–657 (2019).
7. Cogan, S. F. Neural stimulation and recording electrodes. *Annu. Rev. Biomed. Eng.* **10**, 275–309 (2008).
8. Pan, L. et al. Hierarchical nanostructured conducting polymer hydrogel with high electrochemical activity. *Proc. Natl Acad. Sci. USA* **109**, 9287–9292 (2012).
9. Lee, Y. et al. Stretchable organic optoelectronic sensorimotor synapse. *Sci. Adv.* **4**, eaat7387 (2018).
10. Lyu, S. & Untereker, D. Degradability of polymers for implantable biomedical devices. *Int. J. Mol. Sci.* **10**, 4033–4065 (2009).
11. Ratner, B. D., Hoffman, A. S., Schoen, F. J., & Lemons, J. E. *Biomaterials Science: an Introduction to Materials in Medicine* (Elsevier, Academic Press, 2013).
12. Chen, N. et al. Neural interfaces engineered via micro- and nanostructured coatings. *Nano Today* **14**, 59–83 (2017).
13. Rastogi, S. K., Kalmykov, A., Johnson, N. & Cohen-Karni, T. Bioelectronics with nanocarbons. *J. Mater. Chem. B* **6**, 7159–7178 (2018).
14. Yang, W., Thordarson, P., Gooding, J. J., Ringer, S. P. & Braet, F. Carbon nanotubes for biological and biomedical applications. *Nanotechnology* **18**, 412001 (2007).
15. Alkire, R. C., Bartlett, P. N. & Lipkowski, J. *Electrochemistry of Carbon Electrodes* (Wiley, 2015); https://doi.org/10.1002/9783527697489
16. Hansen, S. F. & Lennquist, A. Carbon nanotubes added to the SIN List as a nanomaterial of Very High Concern. *Nat. Nanotechnol.* **15**, 3–4 (2020).
17. Zhu, W. et al. Nanomechanical mechanism for lipid bilayer damage induced by carbon nanotubes confined in intracellular vesicles. *Proc. Natl Acad. Sci. USA* **113**, 12374–12379 (2016).
18. Hwang, J. Y., Li, M., El-Kady, M. F. & Kaner, R. B. Next-generation activated carbon supercapacitors: a simple step in electrode processing leads to remarkable gains in energy density. *Adv. Funct. Mater.* **27**, 1605745 (2017).
19. Zhu, Y. et al. Carbon-based supercapacitors produced by activation of graphene. *Science* **332**, 1537–1541 (2011).
20. Chmiola, J., Largeot, C., Taberna, P. L., Simon, P. & Gogotsi, Y. Monolithic carbide-derived carbon films for micro-supercapacitors. *Science* **328**, 480–483 (2010).
21. Guo, Y. et al. Polymer composite with carbon nanofibers aligned during thermal drawing as a microelectrode for chronic neural interfaces. *ACS Nano* **11**, 6574–6585 (2017).
22. Yin, R. et al. Soft transparent graphene contact lens electrodes for conformal full-cornea recording of electroretinogram. *Nat. Commun.* **9**, 2334 (2018).
23. Chen, X. et al. Stretchable supercapacitors as emergent energy storage units for health monitoring bioelectronics. *Adv. Energy Mater.* **10**, 1902769 (2020).
24. Abbott, J. et al. A nanoelectrode array for obtaining intracellular recordings from thousands of connected neurons. *Nat. Biomed. Eng.* **4**, 232–241 (2020).
25. Tian, B. et al. Macroporous nanowire nanoelectronic scaffolds for synthetic tissues. *Nat. Mater.* **11**, 986–994 (2012).
26. Liu, J. Syringe-injectable electronics. *Nat. Nanotechnol.* **10**, 629–636 (2015).
27. Flores, T., Goetz, G., Lei, X. & Palanker, D. Optimization of return electrodes in neurostimulating arrays. *J. Neural Eng.* **13**, 036010 (2016).
28. Song, B. et al. Solution-processed flexible solid-state micro-supercapacitors for on-chip energy storage devices. In *2015 IEEE 65th Electronic Components and Technology Conference (ECTC)* 1483–1487 (IEEE, 2015); https://doi.org/10.1109/ECTC.2015.7159793
29. Lee, G. et al. High-performance all-solid-state flexible micro-supercapacitor arrays with layer-by-layer assembled MWNT/$MnO_x$ nanocomposite electrodes. *Nanoscale* **6**, 9655–9664 (2014).
30. Pech, D. et al. Ultrahigh-power micrometre-sized supercapacitors based on onion-like carbon. *Nat. Nanotechnol.* **5**, 651–654 (2010).
31. Parameswaran, R. et al. Optical stimulation of cardiac cells with a polymer-supported silicon nanowire matrix. *Proc. Natl Acad. Sci. USA* **116**, 413–421 (2019).
32. Hund, T. J. & Rudy, Y. Determinants of excitability in cardiac myocytes: mechanistic investigation of memory effect. *Biophys. J.* **79**, 3095–3104 (2000).
33. Martersteck, E. M. et al. Diverse central projection patterns of retinal ganglion cells. *Cell Rep.* **18**, 2058–2072 (2017).
34. Ellis, E. M., Gauvain, G., Sivyer, B. & Murphy, G. J. Shared and distinct retinal input to the mouse superior colliculus and dorsal lateral geniculate nucleus. *J. Neurophysiol.* **116**, 602–610 (2016).
35. Jenkins, M. W. et al. Optical pacing of the adult rabbit heart. *Biomed. Opt. Express* **4**, 1626–1635 (2013).
36. Copene, E. D. & Keener, J. P. Ephaptic coupling of cardiac cells through the junctional electric potential. *J. Math. Biol.* **57**, 265–284 (2008).
37. Sperelakis, N. & McConnell, K. Electric field interactions between closely abutting excitable cells. *IEEE Eng. Med. Biol. Mag.* **21**, 77–89 (2002).

## Methods

**Hierarchical porous carbon film preparation.** Resol was prepared by cross-linking of phenol (Sigma-Aldrich) and formaldehyde (Sigma-Aldrich), using methods from the literature[38]. Pluronic block copolymer F127 (template, Sigma-Aldrich) and phenolic resol (carbon source) were mixed at a ratio of 1:2 into an ethanol solution. The precursor solution was stirred for 1 h before use. Vesicle structures were constructed using silica nanosphere templates; 200-nm-diameter silica nanospheres (NanoComposix, 10 mg ml$^{-1}$) were surface modified with a dopamine layer, according to a literature method[39]. The modified nanospheres were then added into precursor solution and mixed until a homogeneous mixture formed. Silicon wafer (Nova Electronic Materials, p-type, 600 nm thermal oxide $SiO_2$) was cut into small pieces with suitable sizes (for example, 2 cm × 4 cm) and cleaned by $O_2$ plasma (Plasma Etcher, PE100) at 100 W for 2 min. The precursor solution with silica nanospheres was spin-coated (Laurell, WS-650 spin coater) onto the surface-cleaned silicon at 1,500 r.p.m. for 45 s. Multiple layers were formed by leaving the silicon wafer at room temperature for 10 min and then repeating the spin-coating. Then pure precursor solution was spin-coated onto the substrate at 3,000 r.p.m. for 45 s. The wafers were kept immobile for 4–6 h at 25 °C, then baked in an oven for 24 h at 100 °C. After baking, the wafers were transferred into an inert argon atmosphere and heated at 700 °C (temperature increase rate of 5 °C min$^{-1}$) for 30 min. The thin film was etched off the silicon wafer, and nanospheres were etched by submerging the wafers in buffered hydrofluoric (Alfa Aesar) acid for 8 h. The thin film was rinsed with deionized water six times and dried prior to further characterizations.

**Device design.** Photomask design was performed in AutoCAD software, and schematics of comb-like devices are shown in Supplementary Fig. 6. The pattern of interdigitated electrodes was consistent in each of the fabricated devices. Electrodes had a width of 15 µm with 10 µm spacing between them and 300 µm distance to the edge of the comb. The single-channel device was composed of 150 pairs of electrodes connected to two large pads, allowing for manual connection to jumper wires. The multi-channel electrode had eight sites arranged in four columns and two rows, and each site had 40 pairs of electrodes. Traces coming from the electrode sites were connected to 16 pads (2.25 mm length, 0.3 mm width, 0.5 mm pitch) matching a zero insertion force connector (FH12A-16S-0.5SH(55), Hirose Electric). SU-8 patterns were designed with perforations in the area outside of the electrodes to increase the surface area available to buffered hydrofluoric acid and to reduce the time required for $SiO_2$ etching. However, we did not notice a notable difference in the fabrication and performance of devices with and without perforations.

**Device fabrication.** A hierarchical porous carbon film obtained on p-type thermal oxide silicon wafer was used as a substrate for fabrication. A standard photolithography procedure was applied to make the desired pattern on the substrate. A schematic of the microfabrication protocol is shown in Supplementary Fig. 6. Metal layers act as a hard mask for reactive-ion etching, and as a conductive and mechanical support for the carbon films. Chromium was used to improve adhesion between material layers; 5 nm Cr, 100 nm Au and 5 nm Cr layers were evaporated on the patterned surface using an electron-beam evaporator (EvoVac, Angstrom Engineering), and extra carbon was removed by reactive-ion etching (Oxford Instruments PlasmaPro, NGP80). The supporting SU-8 layer (SU-8 2015, MicroChem Corp.) had a thickness of approximately 10 µm. Patterns were exposed using a direct writer (MLA150, Heidelberg). The pattern on the SU-8 layer was etched from the substrate with buffered hydrofluoric acid and transferred into deionized water, followed by washing the device with deionized water six times. For free-standing devices, electrodes were transferred onto polyimide film and allowed to dry. For single-site devices, jumper wires were connected to the pads using conducting silver paste (Ted Pella) and after 24 h of drying, the connections and excess of connecting traces were insulated using silicone glue (Kwik-Sil, World Precision Instruments). For multi-site devices, the excess of traces was partially insulated using silicone glue. The connector header was strengthened with polyimide tape, cut to appropriate dimensions and inserted into the zero insertion force connector. For the cell and tissue culture, the devices were directly transferred onto glass microscope slides or into glass-bottom culture dishes. After ensuring even placement, the devices were allowed to dry and partially adhere to the glass. Next, jumper wires were connected using silver paste and left to dry for 24 h, after which the device was fixed to the dish and connections insulated with silicone glue. Devices were sterilized by oxygen plasma (50–100 W for 1 min) and ultraviolet light irradiation before the cell or tissue culture.

**Raman spectroscopy.** Raman spectra were recorded using a LabRAM HR Evolution system (Horiba), and the mapping was done in the ultralow frequency module using a 532 nm laser.

**Electrochemical measurements.** CV was performed over a wide range of scan rates at room temperature or 37 °C in various electrolytes. A potentiostat (SP-200, BioLogic) controlled with EC-Lab software with the three-electrode cell was used. A platinum wire was used as the counter electrode, a Ag/AgCl electrode (1 M KCl) as the reference electrode and a micro-supercapacitor device as the working electrode. Areal cell capacitance ($C$) was calculated from the cathodic phase of CV by $C = \left(\int I\mathrm{d}V\right)/(s\Delta VA)$, where $I$ is the current, $V$ is the potential, $s$ is the scan rate, $\Delta V$ is the potential window and $A$ is the area of the electrode. Galvanic charge/discharge measurements were tested using two symmetric devices in a two-electrode configuration using a source meter (Keithley 2636A, Tektronix) controlled by a LabVIEW program (National Instruments). The voltage shown was the potential between the two symmetric devices. In general, the electrochemical tests were performed without pre-treatment or pre-soak.

**Voltage transients.** Voltage transients were measured using a potentiostat (SP-200, BioLogic) controlled with EC-Lab Express. A platinum wire was used as a counter electrode and a Ag/AgCl (1 M) electrode was used as a reference. For the measurement, the carbon electrode was stabilized at 0 V versus Ag/AgCl for 1 ms in PBS at room temperature. The 700-µs-long cathodic and anodic current pulses were delivered to the electrode with an interpulse delay of 28 µs. The most negative ($E_{mc}$) and positive ($E_{ma}$) polarization potentials were assigned 28 µs after the maximum of a respective peak to account for access voltage and instrument delay. The charge injection limit was taken as a maximum charge injected without exceeding the −0.6 to 0.6 V potential window.

**Electron microscopy.** Transmission electron microscopy (Tecnai F30, FEI) and SEM (Carl Zeiss, Merlin) were used to characterize the hierarchical porous materials and material–cell interfaces. CMs on the materials were fixed in 5% glutaraldehyde PBS solution for 30 min, washed in deionized water and then dehydrated with an increasing ethanol gradient from 30% to 98%. The samples were dried in a critical point dryer (Leica EM CPD300) and observed on the same SEM instrument after coating with an 8 nm Pt/Pd metal layer on a sputter coater (Ted Pella). The SEM instrument was operated at a 2 kV accelerating voltage. Images were analysed using ImageJ.

**Mechanical test.** Indentation modulus and hardness were measured by performing nanoindentation using a Hysitron 950 TriboIndenter in ambient conditions with a Berkovich indenter (three-sided pyramid-shaped diamond tip; tip radius, ~100 nm). All measurements were kept at a constant displacement of 200 nm. The data were analysed using standard Oliver–Pharr method to extract the reduced modulus ($E_r$) and hardness[40]. Specifically, the Young's modulus $E$ of the samples was extracted based on equation (1) (ref. [40]), a general relation that applies to any axisymmetric indenter. For the diamond indenter, the Young's modulus $E_i = 1{,}141$ GPa and the Poisson's ratio $\nu_i = 0.07$ (ref. [41]). Here, we assume the Poisson's ratio of the carbon samples $\nu = 0.25$, which has been widely used for amorphous carbon[42].

$$\frac{1}{E_r} = \frac{1-\nu^2}{E} + \frac{1-\nu_i^2}{E_i} \quad (1)$$

**Finite element simulations.** Finite element analysis was performed using COMSOL Multiphysics software. Details on the modelling of the electric potential and von Mises stress distribution are in Supplementary Notes 1 and 2, respectively.

**Cell culture.** Hearts were excised from neonatal rats (postnatal day 1–3) into ice cold Hank's Balanced Salt Solution (HBSS; without $Ca^{2+}$ or $Mg^{2+}$). The hearts were cut to small (<1 mm) pieces and then rinsed with HBSS to remove blood. A Pierce primary cardiomyocyte isolation kit (Thermo Fisher Scientific) was used for digesting the tissue according to manufacturer protocol. After isolation, the suspended cells were pre-plated for 2 h, allowing fibroblasts to adhere to the tissue culture plate. Then the enriched CM population was seeded onto the micro-supercapacitor device pretreated with fibronectin (Sigma). The cells were allowed to sit in culture media (DMEM high glucose plus 10% fetal bovine serum (FBS), 1% GlutaMAX and 1% penicillin–streptomycin) for 24 h, and then the media was changed to CM-specific media (DMEM high glucose plus 10% FBS, 1% penicillin–streptomycin and 0.1% growth supplement from isolation kit).

**Live–dead viability.** CMs were cultured on the device for three days and then stained with green fluorescent calcein-AM (Life Technologies) and red fluorescent ethidium homodimer-1 (Life Technologies) for 30 min. DAPI was included for nuclear counterstaining in dead cells; 100% EtOH treated cells for 20 min were included as a positive control. The as-stained cells were imaged using a Leica SP5 confocal microscope.

**Nuclear staining assay.** Primary rodent fibroblasts harvested from rat pup hearts (postnatal day 1–3) were seeded and cultured on top of sterilized carbon micro-supercapacitors with fibroblast culture medium (high glucose DMEM plus 10% FBS) for 36 h in an environment of 37 °C and 5% $CO_2$. The seeded device was washed with PBS and then fixed with buffered 4% paraformaldehyde at room temperature. After permeabilization with 0.25% Triton X-100 in PBS, cells were counterstained with Hoechst 33342 (0.1 µg ml$^{-1}$) and imaged on an Olympus inverted fluorescent microscope and Leica Confocal SP5 system. Positive control

samples were prepared by treating fibroblasts with 1 mM hydrogen peroxide to induce apoptosis.

**LDH cytotoxicity assay.** Primary rodent fibroblasts harvested from rat pup hearts (postnatal day 1–3) were seeded and cultured on top of sterilized carbon micro-supercapacitors with fibroblast culture medium (high glucose DMEM plus 10% FBS) in an environment of 37 °C and 5% $CO_2$. The culture medium supernatant was harvested at 24 h (day 1, D1) and 48 h (day 2, D2). LDH activity in the medium supernatant was measured using a Pierce LDH Cytotoxicity Assay Kit (Thermo). Five independent measurements were conducted in each condition. Cycloheximide at the concentration of 10 μg ml$^{-1}$ for 24 h was used to induce cell death as a positive control for this assay. LDH cytotoxicity percentage was calculated by $(LDH_{sample} - LDH_{baseline})/(LDH_{max} - LDH_{baseline}) \times 100\%$, where $LDH_{sample}$ is the corresponding LDH release from the cycloheximide-, device- and SU-8-treated samples; $LDH_{baseline}$ is the spontaneous LDH release activity; and $LDH_{max}$ is the maximum LDH activity detected in whole cell lysates.

**Evaluation of in vivo biocompatibility in mice.** A piece of carbon micro-supercapacitor (0.5 cm × 0.5 cm) was surgically implanted under the dorsal skin of 6- to 8-week-old C57BL/6J mice through incisions, which were later closed with sutures. Mouse body weights were recorded on a weekly basis. At 1 or 4 weeks, mice were euthanized, and skin tissue surrounding the implant site was excised and fixed with buffered formalin for histology. The excised tissues were processed and stained with hematoxylin and eosin for histopathological evaluation at the University of Chicago human tissue resource centre.

**Device connections for the bioelectrical stimulations.** Devices were generally connected in a two-electrode (that is, working electrode and counter electrode) configuration, where the counter electrode was connected to the ground. Square current waveforms (Figs. 3b,e and 4b,f,h (left) and Supplementary Figs. 25, 27 and 28) were delivered using a source meter (Keithley 2636A) controlled using a LabVIEW program. Current pulses (Fig. 4h, middle and right; and Supplementary Fig. 27) were delivered using a potentiostat (SP-200, BioLogic) using EC-Lab Express software. The electric potential was reported as the potential between the two electrodes. In the in vitro cardiac training (Fig. 3b–e and Supplementary Figs. 22–24), the square current waveforms were applied to the two interdigitated electrodes within the same carbon micro-supercapacitor-like device (that is, one interdigitated electrode as the working electrode and the other interdigitated electrode as the grounded counter electrode). In the ex vivo retinal experiments (Fig. 4b), the stimulation of isolated hearts (Fig. 4f,h and Supplementary Figs. 25 and 26) and the stimulation of sciatic nerves (Supplementary Fig. 28), we used two carbon micro-supercapacitor-like devices (that is, with one device as the working electrode, and the other device as the grounded counter electrode). For the traces reported in this Article, the square current waveforms or the current pulses were applied between the two macroscopic devices.

**Calcium imaging.** CMs were treated with calcium sensitive dye (2 μM fluo-4, AM, cell permeant, Thermo Fisher Scientific) for 30 min at 37 °C. Cells were rinsed and incubated for 30 min to allow complete de-esterification. The treated cells were then visualized with a Leica SP5, STED-CW Super-resolution Laser Scanning Confocal. Details of time-series processing from the subthreshold stimulation experiments are described in Supplementary Note 3. Representative videos of normalized change in fluorescence ($\Delta F/F_0$) at the beginning (time, $t = 0$–31.395 s) and at the end ($t = 1{,}900$–$1{,}931.395$ s) of stimulation are attached as Supplementary Videos 1 and 2.

**Immunocytochemistry.** Primary cardiac cells were cultured onto devices for three days and were fixed (4% paraformaldehyde), permeabilized (0.2% Triton X) and then blocked (2% bovine serum albumin (BSA) solution) for an hour to prevent nonspecific binding. Cells were incubated overnight at 4 °C with rabbit anti-cardiac troponin I antibody (1:400 in 2% BSA), chicken anti-vimentin antibody (1:500 in 2% BSA) and mouse Anti-Connexin-43 antibody (1:100 in 2% BSA). Cells were rinsed and subsequently stained for 1 h with Alexa Fluor 488 anti-rabbit, Alexa Fluor 594 anti-chicken and Alexa Fluor 647 anti-mouse secondary antibodies (1:250). DAPI (Invitrogen, P36931) was used to label the nuclei. Stained cells were imaged using the Leica SP5 Confocal and analysed using ImageJ.

**Retina slice.** *Vglut2-IRES-Cre* mice (016963-*Slc17a6*$^{tm2(cre)Lowl}$/*J*) and floxed *Ai95*(*RCL-GCaMP6f*)-*D* mice (028865-*Gt*(*ROSA*)*26Sor*$^{tm95.1(CAG-GCaMP6f)Hze}$/*J*) were acquired fromThe Jackson Laboratory and were crossed to each other in the laboratory of W. Wei to obtain hybrid *Vglut2-IRES-Cre*/*GCaMP6f* transgenic mice. Mice of both sexes (postnatal days 21–35) were used for retinal calcium imaging experiments. Mice were anaesthetized with isoflurane and decapitated after dark adaptation. Under infrared illumination, retinas were isolated from the pigment epithelium in oxygenated Ames' Medium (Sigma-Aldrich, A1420), cut into dorsal and ventral halves, and mounted on filter papers as described in the literature[43]. Retinas were kept in the dark at room temperature in Ames' Medium bubbled with 95% $O_2$ and 5% $CO_2$ until use (0–7 h). Glass coverslips with adhered micro-supercapacitor devices were used as the bottoms of the imaging chamber. During imaging, retinas were placed on top of micro-supercapacitor devices and gently pressed against the surface using a platinum wire weight and perfused with oxygenated Ames' Medium at 32–33 °C. Cells were visualized with infrared light (>900 nm) and an infrared-sensitive video camera (Watec). Calcium transients from GCaMP6f-expressing retinal ganglion cells were recorded by a custom-built two-photon microscope (Bruker) equipped with a Ti–sapphire laser (Chameleon Ultra II, Coherent Technologies) tuned to 920 nm (ref. [44]). Data were acquired using PrairieView software from a 100 μm × 100 μm field of view with an acquisition rate of ~15 Hz. ROIs were manually drawn in ImageJ to enclose the soma of each GCaMP6f-expressing cell and a background region where there was no detectable GCaMP6f expression. Using custom MATLAB scripts, we calculated the average intensity over time for all ROIs and subtracted the background trace from light-responsive somatic traces to remove noise. The calcium traces were resampled to 75 Hz and smoothed using a moving average sliding window of 25 data points (~333 ms). For each stimulation protocol, the average $\Delta F/F_0$ was calculated for every cell.

**Isolated heart.** An adult rat was heparinized (1,000 IU per kilogram body mass, intraperitoneal injection (i.p.)) and anaesthetized using open-drop exposure of isoflurane in a bell jar configuration. The heart was removed and placed in ice cold HBSS buffer, and the aorta was cannulated in preparation for use in a Langendorff set-up. Oxygenated HEPES-buffered Tyrode's solution (containing the following, in mM: NaCl, 126; KCl, 5.4; glucose, 10; HEPES, 10; $MgCl_2$, 1; $CaCl_2$, 2; $MgSO_4$, 1.2; $NaH_2PO_4$, 0.39; bubbled with 99.5% $O_2$; pH, 7.3) was perfused through the cannulated aorta. The perfusion was passed through a heating coil and bubble trap (Radnoti), and the heart was placed in a water-jacketed beaker (Fisher Scientific) to maintain a temperature of 37 °C. The perfusion pressure was maintained at 80–100 mmHg by adjusting the height of the intravenous bag containing the perfusion buffer. The sinoatrial node along with the atria were removed, which resulted in a slow atrioventricular node pace (~1 Hz). The perfusion and LVP were monitored using a BP-100 probe (iWorx) connected to the perfusion line and a water-filled balloon inserted to the left ventricle, respectively. For ECG recordings, needle electrodes were positioned on the LV wall and aorta and connected to a C-ISO-256 preamplifier (iWorx). All signals (perfusion, LVP, and ECG) were amplified using an IA-400D amplifier (iWorx) and interfaced with a computer using a DigiData 1550 digitizer with Clampex software (Molecular Devices). Two devices were placed on the heart: one below the heart's apex, and the other covering the LV wall. Recordings from supercapacitor devices (Supplementary Fig. 29) were achieved with a C-ISO-256 preamplifier (iWorx) as in a regular ECG set-up, but with devices connected as input electrodes.

**In vivo rat nerve stimulation.** Adult rats were deeply anaesthetized with isoflurane (3–4%). The fur was removed from the hindquarters using a surgical clippers and hair removal cream. A semi-circular incision across the midline was made in the skin, and the fascial plane was opened between the gluteus maximus and the anterior head of the biceps femoris, thereby exposing the sciatic nerve. In this setting, two devices were used. One device was placed under the sciatic nerve and the other under the rat's skin.

**Animal subjects.** Mice and rats were housed in the animal facility of the University of Chicago. The animal room was maintained at a humidity of 40–60% and a temperature of 18–23 °C under a 12-h-light/12-h-dark cycle. The animals were allowed free access to food and water. All animal procedures were approved by the Institutional Animal Care and Use Committees of the University of Chicago.

**General data processing.** Analysis of numerical data was performed using Microsoft Excel, OriginPro or Python scripts. Statistical analyses were performed using GraphPad Prism. Plotting was performed using OriginPro, Adobe Illustrator or Python scripts using matplotlib library.

**Reporting Summary.** Further information on research design is available in the Nature Research Reporting Summary linked to this article.

## Data availability

The raw data that support the findings of this study are available from the corresponding authors upon reasonable request. The LabVIEW control program, and the MATLAB and Python scripts are available at https://github.com/uchicago-Tian-Lab/Fang_et_al_Nat_Nanotechnology_2020.

## References

38. Meng, Y. et al. Ordered mesoporous polymers and homologous carbon frameworks: amphiphilic surfactant templating and direct transformation. *Angew. Chem. Int. Ed.* **44**, 7053–7059 (2005).
39. Liu, R. et al. Dopamine as a carbon source: the controlled synthesis of hollow carbon spheres and yolk-structured carbon nanocomposites. *Angew. Chem. Int. Ed.* **50**, 6799–6802 (2011).
40. Oliver, W. C. & Pharr, G. M. Measurement of hardness and elastic modulus by instrumented indentation: advances in understanding and refinements to methodology. *J. Mater. Res.* **19**, 3–20 (2004).

41. Li, X. & Bhushan, B. A review of nanoindentation continuous stiffness measurement technique and its applications. *Mater. Charact.* **48**, 11–36 (2002).
42. Suk, J. W., Murali, S., An, J. & Ruoff, R. S. Mechanical measurements of ultra-thin amorphous carbon membranes using scanning atomic force microscopy. *Carbon* **50**, 2220–2225 (2012).
43. Wei, W., Elstrott, J. & Feller, M. B. Two-photon targeted recording of GFP-expressing neurons for light responses and live-cell imaging in the mouse retina. *Nat. Protoc.* **5**, 1347–1352 (2010).
44. Denk, W. & Detwiler, P. B. Optical recording of light-evoked calcium signals in the functionally intact retina. *Proc. Natl Acad. Sci. USA* **96**, 7035–7040 (1999).

## Acknowledgements

This work is supported by the National Institutes of Health (NIH NS101488), Army Research Office (W911NF-18-1-0042), National Science Foundation (NSF CMMI-1848613) and Office of Naval Research (PECASE, N000141612958).

## Author contributions

Y.F. and B.T. conceived the concept of this manuscript. Y.F., A.P. and L.M. fabricated the carbon micro-supercapacitor-like devices. Y.L., A.P. and Y.F. conducted the electrochemistry characterizations. A.P. and L.M. conducted the COMSOL simulations. Y.F. and A.P. performed the in vitro cardiac pacing experiments. M.Y.R., A.P. and L.M. conducted the isolated heart experiments. H.A.L. and W.W. conducted the retina stimulation experiments. A.P., L.M., J.Y., M.Y.R. and B.E. conducted the nerve stimulation experiments. J.Y. and Y.F. conducted the in vitro and in vivo biocompatibility experiments. E.S. and N.Y. assisted in the in vitro culture and imaging. J.J., E.S. and Y.J. helped with data analysis. All authors contributed to the preparation of the manuscript.

## Competing interests

The authors declare no competing interests.

## Additional information

**Supplementary information** is available for this paper at https://doi.org/10.1038/s41565-020-00805-z.

**Correspondence and requests for materials** should be addressed to Y.F. or B.T.

**Peer review information** *Nature Nanotechnology* thanks the anonymous reviewers for their contribution to the peer review of this work.

**Reprints and permissions information** is available at www.nature.com/reprints.

nature research

Corresponding author(s): Bozhi Tian and Yin Fang

Last updated by author(s): Oct 18, 2020

# Reporting Summary

Nature Research wishes to improve the reproducibility of the work that we publish. This form provides structure for consistency and transparency in reporting. For further information on Nature Research policies, see our Editorial Policies and the Editorial Policy Checklist.

## Statistics

For all statistical analyses, confirm that the following items are present in the figure legend, table legend, main text, or Methods section.

| n/a | Confirmed | |
|---|---|---|
| ☐ | ☒ | The exact sample size (*n*) for each experimental group/condition, given as a discrete number and unit of measurement |
| ☐ | ☒ | A statement on whether measurements were taken from distinct samples or whether the same sample was measured repeatedly |
| ☐ | ☒ | The statistical test(s) used AND whether they are one- or two-sided<br>*Only common tests should be described solely by name; describe more complex techniques in the Methods section.* |
| ☐ | ☒ | A description of all covariates tested |
| ☐ | ☒ | A description of any assumptions or corrections, such as tests of normality and adjustment for multiple comparisons |
| ☐ | ☒ | A full description of the statistical parameters including central tendency (e.g. means) or other basic estimates (e.g. regression coefficient) AND variation (e.g. standard deviation) or associated estimates of uncertainty (e.g. confidence intervals) |
| ☐ | ☒ | For null hypothesis testing, the test statistic (e.g. *F*, *t*, *r*) with confidence intervals, effect sizes, degrees of freedom and *P* value noted<br>*Give P values as exact values whenever suitable.* |
| ☒ | ☐ | For Bayesian analysis, information on the choice of priors and Markov chain Monte Carlo settings |
| ☐ | ☒ | For hierarchical and complex designs, identification of the appropriate level for tests and full reporting of outcomes |
| ☒ | ☐ | Estimates of effect sizes (e.g. Cohen's *d*, Pearson's *r*), indicating how they were calculated |

*Our web collection on statistics for biologists contains articles on many of the points above.*

## Software and code

Policy information about availability of computer code

**Data collection**

Cyclic voltammetry (CV) a potentiostat (SP-200, BioLogic) with EC-Lab software (v. 1.33, BioLogic). Galvanostatic charge/discharge were measured using a source meter (Keithley 2636A, Tektronix, Inc.) where control and data acquisition were performed using custom LabVIEW program (v. 2013 13.0.1, National Instruments). Voltage transients were measured using a potentiostat (SP-200, BioLogic) with EC-Lab Express software (v. 5.56, BioLogic).

For in vitro experiments, square current waveforms were delivered using a source meter (Keithley 2636A, Tektronix, Inc.) where control and data acquisition were performed using custom LabVIEW program (v. 2013 13.0.1, National Instruments). Time base for control and data acquisition set in LabView program was approximately 50 ms.

Left ventricular pressures (LVP) and perfusion pressure were monitored using a BP-100 probe (iWorx). ECG and EMG recordings were acquired using a C-ISO-256 preamplifier (iWorx). Perfusion, LVP, ECG and EMv. G signals were amplified using an IA-400D amplifier (iWorx) and interfaced with a PC using a DigiData 1550 digitizer using Clampex software (v. 10.4.0.36, Molecular Devices). Current pulses were delivered using a potentiostat (SP-200, BioLogic) controlled using EC-Lab Express software (v. 5.56, BioLogic). To synchronize time base between instruments during stimulation experiments, TTL signal was sent from DigiData 1550 digitizer to SP-200 Analog 1 input. Time base of data acquisition was 100 µs for DigiData 1550 and 140 µs for SP-200.

Data from custom-built two-photon microscope (Bruker) equipped with a Ti:sapphire laser (Chameleon Ultra II; Coherent Technologies) tuned to 920 nm was acquired using PrairieView 5.4 (Bruker).

COMSOL Multiphysics 5.5 software was used for simulations.

**Data analysis**

Analysis of numerical data was performed using Microsoft Excel for Office 365 (v.16.0), OriginPro 2016 (v. 9.3) or Python (v. 3.7.4) scripts. Statistical analyses were performed using GraphPad Prism (v. 8.4.3). Plotting was performed using OriginPro2016 (v. 9.3), Adobe Illustrator (24.3) or Python (v. 3.7.4) scripts using matplotlib library (v. 3.1.1). Confocal microscope images and imaging data were processed and

analyzed using Leica LAS AF Lite and ImageJ (Fiji, v. 2.0.0-rc-68). The average intensities in retina experiment were processed using custom MATLAB 2019b scripts for calculation and background subtraction. The pacing frequencies in subthreshold stimulation experiment were analyzed using Python (v. 3.7.4) script using methods described in Supplementary Information. Electron microscopy data were analyzed using ImageJ (Fiji, v. 2.0.0-rc-6). EDX data were processed using AZtec (v. 4.3, Oxford Instruments). Photomasks were designed in AutoCAD 2017.1.2.

For manuscripts utilizing custom algorithms or software that are central to the research but not yet described in published literature, software must be made available to editors and reviewers. We strongly encourage code deposition in a community repository (e.g. GitHub). See the Nature Research guidelines for submitting code & software for further information.

## Data

Policy information about availability of data

All manuscripts must include a data availability statement. This statement should provide the following information, where applicable:

- Accession codes, unique identifiers, or web links for publicly available datasets
- A list of figures that have associated raw data
- A description of any restrictions on data availability

Raw data used in this study are available upon reasonable request. LabVIEW control program, and MATLAB and Python scripts are available at https://github.com/uchicago-Tian-Lab/Fang_et_al_Nat_Nanotechnology_2020.

# Field-specific reporting

Please select the one below that is the best fit for your research. If you are not sure, read the appropriate sections before making your selection.

☒ Life sciences ☐ Behavioural & social sciences ☐ Ecological, evolutionary & environmental sciences

For a reference copy of the document with all sections, see nature.com/documents/nr-reporting-summary-flat.pdf

# Life sciences study design

All studies must disclose on these points even when the disclosure is negative.

| | |
|---|---|
| Sample size | Sample size was not calculated beforehand. Sample size was determined based on extensive laboratory experience and literature in the field. The number of biological replicates we aimed for was at least 3 with technical replicates in each group so that the number of biological and technical replicates is necessary to convince us that the effect was real. Specific sample size has been indicated in the figure legends. |
| Data exclusions | Representative images were shown in the manuscripts; similar results from experimental repeats were not shown. No data excluded for statistical analyses. |
| Replication | All experimental findings were reliably reproduced and each experiment was reproduced with similar results. Reproducibility has been indicated in the figure legends. |
| Randomization | The same type of materials, cells and animals were used for all experiments and for all experiments, animals were randomly assigned to groups. For biological images, cells were examined at several random locations. |
| Blinding | Experimenters were blinded during imaging experiments. Biocompatibility tests and stimulation experiments were not performed blind to the conditions of the experiments as treatments were determined beforehand and animal were selected in order to acquire sufficient sample size per experimental group. All subsequent sample processing was done blinded. |

# Reporting for specific materials, systems and methods

We require information from authors about some types of materials, experimental systems and methods used in many studies. Here, indicate whether each material, system or method listed is relevant to your study. If you are not sure if a list item applies to your research, read the appropriate section before selecting a response.

## Materials & experimental systems

| n/a | Involved in the study |
|---|---|
| ☐ | ☒ Antibodies |
| ☐ | ☒ Eukaryotic cell lines |
| ☒ | ☐ Palaeontology and archaeology |
| ☐ | ☒ Animals and other organisms |
| ☒ | ☐ Human research participants |
| ☒ | ☐ Clinical data |
| ☒ | ☐ Dual use research of concern |

## Methods

| n/a | Involved in the study |
|---|---|
| ☒ | ☐ ChIP-seq |
| ☒ | ☐ Flow cytometry |
| ☒ | ☐ MRI-based neuroimaging |

## Antibodies

Antibodies used

Immunostaining:
Primary antibodies: Rabbit anti-cardiac troponin I antibody (Abcam ab47003, 1:400); chicken anti-vimentin antibody (Abcam ab24525, 1:500); mouse anti-Connexin 43 antibody (Sigma Aldrich MAB3067, 1:100).
Secondary antibodies: Alexa Fluor 488 - labeled goat anti-rabbit IgG (H+L) (1: 250, A-11008, Life Technologies); Alexa Fluor 594 - labeled goat anti-chicken IgY (H+L) (1: 250, A-32759, Life Technologies); Alexa Fluor 647 - labeled goat anti-mouse IgG (H+L) (1: 250, A-28121, Life Technologies);
Detailed product information is available on the company's website.

Validation

Immunostaining antibodies:
Chicken anti-Vimentin antibody has been validated by western blots and immunofluorescence staining, and reacts with vimentin from a wide range of species, including rat, mouse, and human. Totally 52 references are available for this antibody. Detailed information is available on the company's website.

Rabbit anti-cardiac troponin I polyclonal antibody has been validated by western blots and immunofluorescence staining, and reacts with troponin I from a wide range of species, including rat, mouse, human and pig. Totally 77 references are available for this antibody. Detailed information is available on the company's website.

Mouse anti-connexin-43 antibody has been validated by western blots and and immunofluorescence staining, and reacts with connexin-43 from a wide range of species, including rat, mouse, human, pig, and canine. More than 80 references are available for this antibody. Detailed information is available on the company website.

## Eukaryotic cell lines

Policy information about cell lines

Cell line source(s)

Primary rat cardiac fibroblasts (RCFs) and primary cardiomyocytes were isolated from hearts that excised from P0-5 neonatal rats. A Pierce™ primary cardiomyocyte isolation kit (Thermo Fisher Scientific) was used for digesting the tissue according to manufacturer protocol.

Authentication

primary cardiomyocytes were authenticated with immunofluorescence staining against cardiomyocyte markers including cardiac troponin and connexin-43. Primary rat cardiac fibroblasts were authenticated with staining against vimentin.

Mycoplasma contamination

All cell lines were tested negative for mycoplasma contamination with Venor™ GeM Mycoplasma Detection Kit (Sigma, #MP0025)

Commonly misidentified lines
(See ICLAC register)

No commonly misidentified cell lines were used.

## Animals and other organisms

Policy information about studies involving animals; ARRIVE guidelines recommended for reporting animal research

Laboratory animals

Transgenic mice (Slc17a6tm2(cre)Lowl/Gt(ROSA)26Sortm95.1(CAG-GCaMP6f)Hze) expressing the calcium indicator GCaMP6 were used in retina experiments.

6-8 week old C57BL/6J mice (female and male) were used in in vivo biocompatibility experiments (H&E staining, and body weight).

Neonatal (P1-P3) Sprague-Dawley rats (female and male) from Charles River Laboratories were used for primary rat cardiac fibroblasts (CFs) and primary cardiomyocyte in vitro experiments.

Adult (10-16 weeks) Sprague-Dawley rats (female and male) from Charles River Laboratories were used for heart and nerve stimulations.

Mice and rats were housed in the animal facility of the University of Chicago. The animal room was maintained in an environment with the humidity of 40-60 % and the temperature of 18-23°C under a 12-h light/12-h dark cycle. The animals were allowed free access to food and water.

Wild animals

No wild animals were used.

Field-collected samples

No field-collected samples were used.

Ethics oversight

All animals were housed under pathogen-free conditions and all animal procedures were approved by the Institutional Animal Care and Use Committees (IACUC) of the University of Chicago.

Note that full information on the approval of the study protocol must also be provided in the manuscript.